Research Article Vol. 30, No. 23 / 7 Nov 2022 / *Optics Express* 41118

Optics EXPRESS

Phase-resolved all-fiber reflection-based *s*-NSOM for on-chip characterization

YIZHI SUN,[1] XIAOHONG YAN,[2,3] SYLVAIN BLAIZE,[4]
RENAUD BACHELOT,[4] HONG WEI,[2,5] AND WEI DING[1,*]

[1] *Guangdong Provincial Key Laboratory of Optical Fiber Sensing and Communication, Institute of Photonics Technology, Jinan University, Guangzhou 511443, China*
[2] *Institute of Physics, Chinese Academy of Sciences, Beijing 100190, China*
[3] *School of Physical Sciences, University of Chinese Academy of Sciences, Beijing 100049, China*
[4] *Light, Nanomaterials, Nanotechnologies (L2n), Institut Charles Delaunay, CNRS, Université de Technologie de Troyes, Troyes 10004, France*
[5] *Songshan Lake Materials Laboratory, Dongguan 523808, China*
[*] *dingwei@jnu.edu.cn*

Abstract: We report on a phase-resolved, reflection-based, scattering-type near-field scanning optical microscope technique with a convenient all-fiber configuration. Exploiting the flexible positioning of the near-field probe, our technique renders a heterodyne detection for phase measurement and point-to-point frequency-domain reflectometry for group index and loss measurement of waveguides on a chip. The important issue of mitigating the measurement errors due to environmental fluctuations along fiber-optic links has been addressed. We perform systematic measurements on different types of silicon waveguides which demonstrate the accuracy and precision of the technique. With a phase compensation approach on the basis of a common-path interferometer, the phase drift error is suppressed to ∼ 0.013°/s. In addition, characterizations of group index, group velocity dispersion, propagation loss, insertion loss, and return loss of component waveguides on a chip are all demonstrated. The measurement accuracy of the propagation loss of a ∼ 0.2 cm long nano-waveguide reaches ±1 dB/cm. Our convenient and versatile near-field characterization technique paves the way for in-detail study of complex photonic circuits on a chip.

© 2022 Optica Publishing Group under the terms of the Optica Open Access Publishing Agreement

1. Introduction

Near-field scanning optical microscopy (NSOM) with spatial resolution below the diffraction limit [1–3] is a powerful technique for investigating on-chip nanophotonic devices that feature complex field profiles and multiple scales [4–11]. Compared to the “black-box-type” measuring techniques [12–15], NSOM gains merit in two aspects. Firstly, a NSOM probe can be deployed to any place, and a piezoelectric position control can minimize the location uncertainty relative to the sample of a sub-nanometer level [16]. Secondly, the geometry and material composition of a NSOM tip can be deliberately altered for measurement of different electromagnetic field components [17–25].

Thanks to the use of sharply-ended atomic force microscope (AFM) tips of ∼20 nm size, a scattering-type NSOM (*s*-NSOM) usually surpasses an aperture NSOM in terms of resolution. Furthermore, by introducing a transmission-based or reflection-based measuring configuration [26–28] into a *s*-NSOM for the characterization of on-chip photonic devices, the tedious alignment task in a free-space counterpart [29,30] can be substantially reduced, allowing one to build setups with a convenient all-fiber form and low background noise. In such setups, the waveguide itself plays the role of a high-numerical-aperture lens for efficient light collection. Amongst the transmission and reflection configurations, the latter one has an additional merit that the signal light carries more information of interest, such as propagation phase, delay, and loss.

#475192 https://doi.org/10.1364/OE.475192
Journal © 2022 Received 7 Sep 2022; revised 12 Oct 2022; accepted 12 Oct 2022; published 24 Oct 2022

To further exploit the reflection-based *s*-NSOM technique and acquire more properties of on-chip waveguides, the main obstacle lies in the conventional raster-scanning mode with long measurement durations and short scanning ranges. Firstly, since the phase measurement with a heterodyne or pseudo-heterodyne manner [29–31] needs a Mach-Zehnder (or Michelson) interferometer, and optical fibers have intrinsic thermal and stress sensitivities [32], the phase acquisition in an all-fiber setup will suffer with severe drift during a process of several minutes. Further, although the near-field probe can be arbitrarily positioned across a chip, the raster-scanning with high lateral accuracy is only restricted in a range of ~100 μm, which makes it difficult to measure the loss, group index, and group velocity dispersion of a waveguide with typical length of a few millimeters.

In this work, we manage to combine the high-stability phase measurement and the loss, group index, and dispersion measurement of on-chip waveguides in a convenient all-fiber *s*-NSOM setup. Heterodyne detection is realized with an in-line phase modulator, and a very low phase drift of ~ 0.013°/s is attained in experiment. The point-to-point near-field characterization [33,34] along a waveguide and optical frequency-domain reflectometry (OFDR) at each site [14,35–37] allow us to measure the loss and the group index of any segment of waveguide and of different orders of mode. The accuracy of our loss measurement comes from the adoption of a new measurand, which is insensitive to fiber-to-chip coupling, and the precise positioning of AFM tip. The loss measurement uncertainty is validated to be ±1 dB/cm for a ~ 0.2 cm long waveguide.

2. Measurement principle

The upper right corner of Fig. 1 outlines a reflection-based *s*-NSOM, consisting of an AFM module (NT-MDT SI, Solaris) and a fiber circulator. The silicon AFM probe (Scansens, HA_NC) with tip radius of ~10 nm and full cone angle of ~30° (therefore a ~20 nm spatial resolution) gets access to near field in tapping mode with the dither frequency of $\Omega \approx 140$ kHz and the vibration amplitude of ~100 nm. The light-tip interaction converts part of the near field to the guided waves in the backward direction, constituting a modulated optical signal [28].

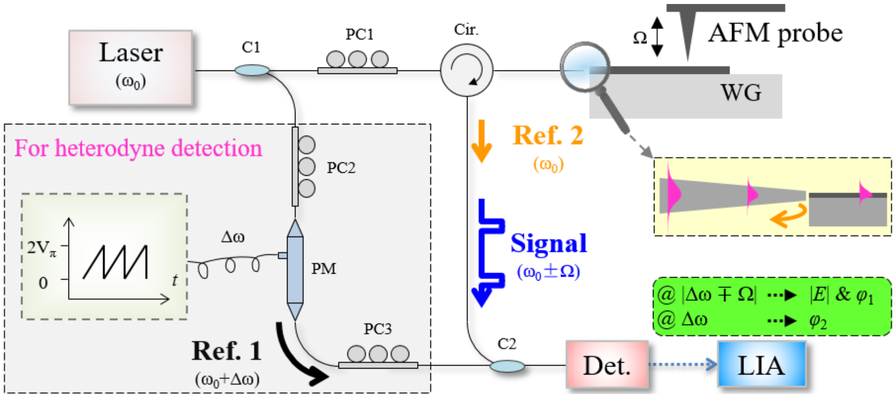

Fig. 1. Schematic of heterodyne detection of optical signals in a reflection-based s-NSOM. C1/C2, 50:50 directional couplers; PC1-3, polarization controllers; Cir., circulator; WG: waveguide under test; PM, phase modulator; V_π, half-wave voltage; Det., photodetector; LIA, lock-in amplifier.

2.1. Heterodyne detection in a fiber interferometer

To retrieve the amplitude and phase information of the reflected light, heterodyne detection on the basis of a fiber Mach-Zehnder interferometer is conducted. As shown in Fig. 1, a continuous wave (CW) light (with the frequency of ω_0) from a tunable laser source (Agilent, 81940A, with the line-width of <100 kHz and the wavelength ranging from 1520 to 1630 nm) is launched into a waveguide under test via a lensed fiber (CXFIBER). In this signal arm, the reflected light is amplitude-modulated by the AFM tip (at Ω), thus generating two frequency-shifted tones of $\omega_0 \pm \Omega$. In the reference arm, the light transmits a $LiNbO_3$ phase modulator (SWT Sci. & Tech.), which is driven by a saw-tooth waveform, and forms a frequency-shifted beam (referred to as Ref. 1 with the frequency of $\omega_0 + \Delta\omega$ and $\Delta\omega \approx 30$ kHz). After the signal and the reference beams combine inside an InGaAs photodetector (Thorlabs, PDA10CS2), the photocurrent is demodulated (at $|\Delta\omega \mp \Omega|$) by a digital lock-in amplifier (Zurich Instruments, HF2LI), yielding the amplitude ($|E|$) and phase (φ_1).

For a fiber interferometer, the main challenge of measurement accuracy is the phase drift originating from environmental fluctuations [38–40]. Considering a single-mode silica optical fiber with the thermal phase sensitivity of ~47 rad/m/°C at telecom wavelengths [32] and a fiber length of a few meters, the variation of the ambient temperature (~1 °C) during a measurement lasting for several minutes can bring about severe phase drift of ~100 rad. To mitigate this issue, many methods have been reported, including to equalize the fiber lengths of the two arms [38], to enclose the setup inside an incubator [39], etc. In this work, we adopt the common-path interferometer (CPI) method [28]. As depicted in the zoom-in panel of Fig. 1, the reflected light at the front facet of the waveguide (~1% of the launch light) can be utilized as a calibration beam (Ref. 2, with the frequency of ω_0). The phase difference (φ_2) between the beams of Ref. 1 and Ref. 2 can be demodulated with the frequency of $\Delta\omega$. All the accumulated phase drift across optical fibers can therefore be eliminated in the measurement of φ_1 - φ_2. The residual phase drift may come from the thermo-optic effect in the waveguide.

2.2. Near-field optical frequency-domain reflectometry

Regarding near-field optical characterizations, the amplitude and phase mapping within a single raster-scanning frame of a *s*-NSOM can benefit from a high lateral resolution [3,16]. However, due to the short scan range of a piezoelectric stage, such measurements cannot expand beyond the scale of ~100 µm. To overcome this shortcoming, especially for the loss measurement of a waveguide, we adopt OFDR in our setup and analyze the propagation delay information point by point.

Returning back to the homodyne detection setup (i.e., Fig. 1 excluding the dash box), the demodulated signal η (at the dither frequency of the AFM probe of Ω) from the photocurrent curve represents the interference between the Ref. 2 (reflected light at the front facet of the waveguide) and the Signal (reflected light by the AFM tip) beams [28]. As shown in Fig. 2, in a more detailed analysis [37], the Signal beam can be decomposed to two major components. One is from the direct reflection at the AFM tip (Signal 1), and the other is from the extinction of the propagating light (Signal 2). The extinction light is then back-reflected by a reflection plane behind the AFM tip (e.g., the rear facet of the waveguide). Note that in this work we only count the extinction action once along each light propagation, because the signals arising from multiple light–probe interactions are too weak to be detected [37]. As outlined in Fig. 2, the extinction light (Signal 2) can be produced via two routes, corresponding to the two different sequences of the tip extinction and the plane reflection interactions. The black solid line and the purple dash line labeled for Signal 2 (see Fig. 2) delineate the light before and after the probe induced extinction, respectively.

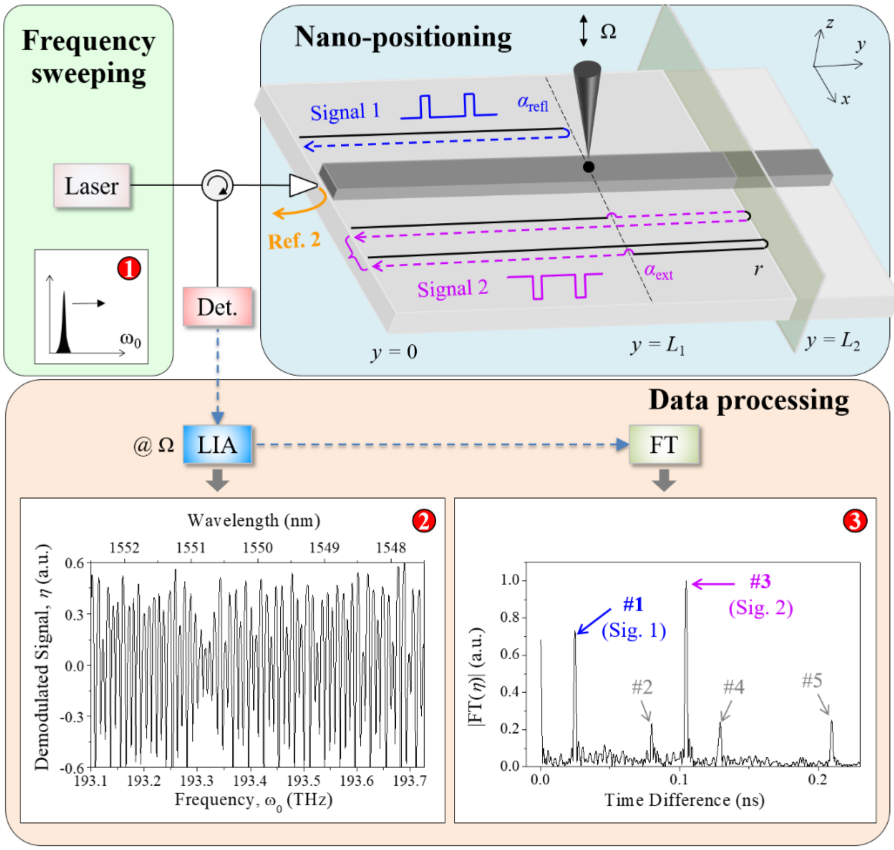

Fig. 2. Schematic of near-field OFDR measurement. Inset 1: Illustrative spectrum of a laser. Inset 2: A typical spectrogram of the demodulated signal η. Inset 3: The amplitude of FT of the η spectrum in Inset 2.

Accordingly, the amplitudes of Signal 1 and Signal 2 can be expressed as

$$|E_{\text{Sig1}}| = |E_0| \cdot \alpha_0 \alpha_{\text{refl}} \cdot e^{-2\alpha L_1} \tag{1a}$$

and

$$|E_{\text{Sig2}}| = 2|E_0| \cdot r \cdot \alpha_0 \alpha_{\text{ext}} \cdot e^{-2\alpha L_2}, \tag{1b}$$

respectively. Here, $|E_0|$ stands for the optical amplitude of the laser. L_1 and L_2 are the waveguide distances relative to the positions of the AFM tip and the reflection plane, respectively. α is the amplitude propagation attenuation of the waveguide. α_{refl} and α_{ext} are the amplitude coefficients of the light reflection and extinction at the AFM tip (see Appendix A for detailed simulations), respectively, and are a function of polarization, waveguide size, and AFM tip location. r stands for the amplitude reflection coefficient at the reflection plane (behind the AFM tip). α_0 contains all the other attenuation factors in the circuit, including the losses of all the fiber devices and the fiber-to-waveguide coupling loss. The factor 2 in Eq. (1b) arises from the two possible sequences to produce Signal 2, as mentioned above.

According to Eq. (1a), $|E_{\text{Sig1}}|$ contains the information of the AFM tip location (L_1) and the loss (α), thus indicating that the loss measurement can be implemented by quantifying $|E_{\text{Sig1}}|$ at different L_1's. For this end, the first issue of the limited scan range of a NSOM stage (~100 μm) can be resolved by cruising the AFM tip along the waveguide. While, the second issue for loss measurement, which may be more challenging, is how to reduce (minimize) the variation of α_0 during point-to-point measurements. This problem becomes severe when taking into account both fluctuations of the laser power and the fiber-to-waveguide coupling. In experiment, we adopt a new measurand of

$$|E_\mathrm{r}| \equiv |E_\mathrm{Sig1}|/|E_\mathrm{Sig2}| = \alpha_\mathrm{refl}/(2r\alpha_\mathrm{ext}) \cdot e^{2\alpha(L_2-L_1)}, \tag{2}$$

where both factors of $|E_0|$ and α_0 are cancelled out. And, if the values of $\alpha_\mathrm{refl}/(2r\alpha_\mathrm{ext})$ and L_2 keep invariant during measurement (see Appendix A), $|E_\mathrm{r}|$ will be only relevant to α and L_1.

From Eq. (2), it is manifest that the parameters L_1, L_2, and $|E_\mathrm{r}|$ are required for deriving the propagation attenuation α. This can be implemented by an OFDR technique. As the frequency of the laser sweeps (see Inset 1 of Fig. 2) and an AFM tip lays upon the waveguide, the inset 2 of Fig. 2 shows a representative η spectrogram. Employing Fourier transform (FT) to the η spectrum [35,37], the peaks #1 and #3 (corresponding to Signals 1 and 2, respectively) appear, as shown in Inset 3 of Fig. 2. In the same manner, the other peaks in Inset 3 can also be identified to multiply-reflected lights inside the waveguide [37]. L_1 and L_2 can then be extracted according to a priori group index of the propagation mode (by numerical simulation or measurement). In addition, the ratio of the heights of these two peaks refers to as $|E_\mathrm{r}|$.

Indeed, the group index of the propagation mode can also be deduced from a low-coherence interferometry [41]. To do so, we first filter out peaks #1 (Signal 1) from the FT(η) spectrum, take inverse FT, and then give out the propagation phase as a function of the wavelength. With a known distance L_1 (e.g., by placing the AFM tip at a certain position of the waveguide), the phase spectrum can give rise to group index and group velocity dispersion. Detailed results will be described in the next section.

3. Experiments

In this section, a number of applications of the proposed measurement technique will be tested. Our sample waveguides are fabricated on a silicon-on-insulator (SOI) wafer (Soitec), composed of a 220-nm-thick crystalline Si layer and a 2-µm-thick buried oxide layer over a Si substrate. The fabrication process includes the standard deep-UV lithography and reactive ion etching with no top cladding. All the waveguides are arranged on a 4 mm × 8 mm chip, whose input and output end facets are fine polished.

3.1. Near-field imaging with phase drift compensation

As shown in Fig. 3(a), a straight SOI waveguide is composed of a 500 nm × 220 nm nano-waveguide in the middle (Inset 1), two 2 µm × 220 nm waveguides on both ends, and two linear tapers in between. The lengths of the five segments are 2.45 mm (the nano-waveguide), 0.8 mm/0.65 mm (the waveguides on both ends), and 50 µm (the two linear tapers), respectively. According to a finite element method (FEM) simulation, the nano-waveguide can support two guided modes at 1550 nm, including a quasi-TM mode [Inset 2 of Fig. 3(a)] which cuts off at ~1650 nm.

To demonstrate the low-phase-drift attribute of our measuring technique, an AFM tip is laid upon the midpoint of the nano-waveguide at one site. In a comparative test, two measurements with and without phase compensation (φ_1 - φ_2 *vs* φ_1) manifest a huge difference [Fig. 3(b)]. The phase drift rate of φ_1 is measured to be greater than 5 °/s, probably caused by a ~2 m long fiber difference [39] with the consideration of a thermal phase sensitivity of ~ 47 rad/m/°C [32] and a representative room temperature varying rate of ~0.001 °C/s. Conversely, with the phase compensation, the phase drift rate dramatically drops to ~0.013 °/s. This >2 orders of magnitude of phase-drift-error reduction achieved in our all-fiber interferometer [Fig. 3(c)] should be attributed to both adoption of the CPI setup [28] and our efforts to stabilize room temperature

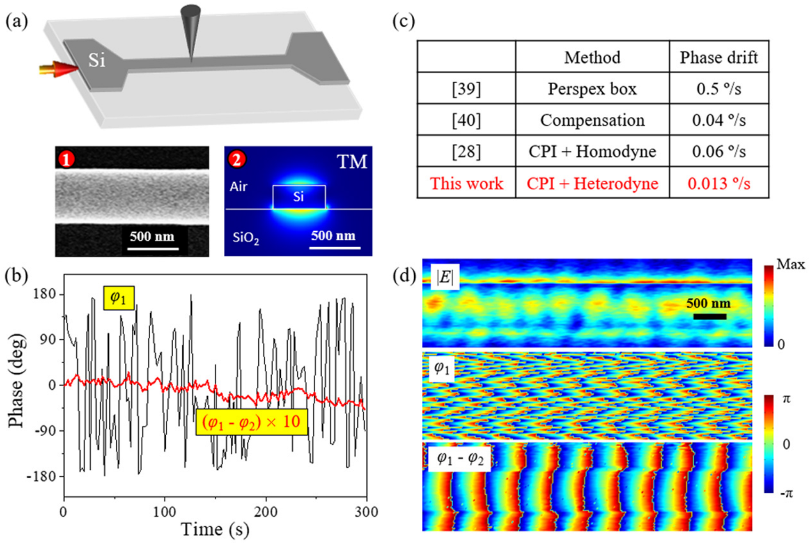

	Method	Phase drift
[39]	Perspex box	0.5 °/s
[40]	Compensation	0.04 °/s
[28]	CPI + Homodyne	0.06 °/s
This work	CPI + Heterodyne	0.013 °/s

Fig. 3. (a) Schematic of a SOI nano-waveguide with both ends connected with two multi-mode waveguides via linearly-tapered transitions. Inset 1: Scanning electron microscopy (SEM) image of the nano-waveguide. Inset 2: FEM simulated TM mode profile of $|E|^2$ at 1550 nm. (b) Phase measurements at a certain point atop the nano-waveguide with (red) and without (black) the CPI *plus* heterodyne phase compensation. (c) Comparison of phase drift rates of different techniques. (d) Amplitude ($|E|$) and phase distributions without (φ_1) and with (φ_1-φ_2) compensation of the TM-mode at 1550 nm.

and air flow. The remainder phase drift (of 0.013 °/s) may be from the thermal phase sensitivity of silicon (~ 770 rad/m/°C [42]) and the ~1 mm length of the silicon waveguide between the input end and the measurement site.

Also, Fig. 3(d) presents the amplitude and phase distributions of a forwardly-propagating (from left to right) quasi-TM wave at 1550 nm with each raster scan operation lasting for ~200 seconds. Again, the phase compensation method (φ_1-φ_2) validates high validity to overcome environmental fluctuations. In our measurements, the one-way propagation of the guided wave is enabled by a low reflectivity at the rear facet of the waveguide [~14% according to finite difference time domain (FDTD) calculation] and a high propagation loss of the quasi-TM mode. Nevertheless, the $|E|$ profile in Fig. 3(d) still reveals some feature of weakly-standing wave.

The phase-stabilized near-field imaging can also help to distinguish the modes of different orders. Figure 4(a) shows the amplitude and phase distributions at 1550 nm when a TM-polarized light is launched into a 2 µm × 220 nm multi-mode waveguide. Applying FT to the near-field profile of each row yields three discrete effective indices of 1.76, 1.71, and 1.61, corresponding to the quasi-TM$_{00}$, TM$_{01}$, and TM$_{02}$ modes respectively. The transverse profiles of these three modes can also be displayed after Fourier analysis [Fig. 4(b,c)].

3.2. Group index and group velocity dispersion measurement

Our technique is suited to measure group index and group velocity dispersion. The light reflected by the AFM tip contains the information of propagation delay, which varies as the wavelength and the order of the mode change.

In experiment, at two successive sites of a 500 nm × 220 nm nano-waveguide [Fig. 5(a)], we carry out frequency sweeping with the rate of 0.5 nm/s, collect the demodulated signal η, perform FT to the η spectrum, filter out the peak of Signal 1 (see Inset 3 of Fig. 2), and then

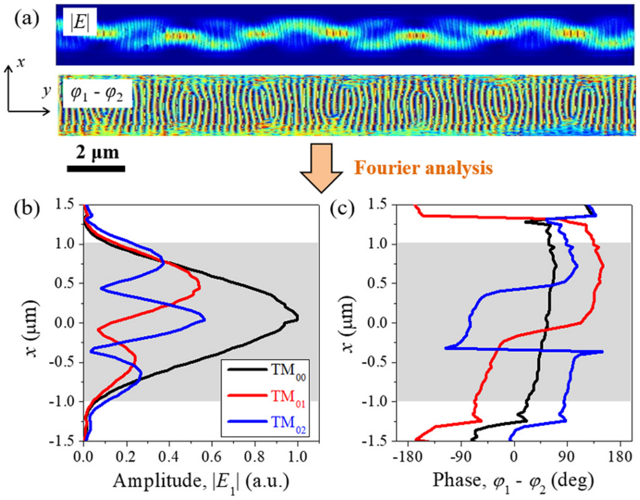

Fig. 4. (a) Measured near-field amplitude and phase profiles of the TM waves in a 2 µm × 220 nm SOI waveguide at 1550 nm. (b,c) Transverse amplitude and phase profiles of these three TM modes.

inversely FT it to a η curve (η_{Sig1}). For the TE and TM modes, and with the AFM tip precisely at the midpoints of the waveguide, the η_{Sig1} spectra ranging from 1530 to 1620 nm are presented in Fig. 5(b). The distance between the two measuring sites is about 2.45 mm.

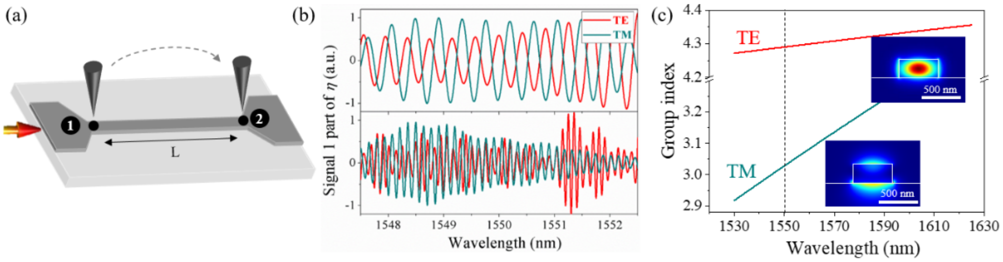

Fig. 5. (a) Sketch of group index and group velocity dispersion measurement of a nano-waveguide by successively probing at two sites. (b) Signal 1 parts of the η spectra measured at the two sites and with two polarizations. (c) Derived group indices of the TE (red) and TM (dark green) modes.

Considering that the η_{Sig1} spectra are only relevant to the interference of Ref. 2 and Signal 1, these spectral-domain low-coherence interferograms [41] allow us to derive group index and dispersion. As displayed in Fig. 5(c), the group indices of the TE and TM modes at 1550 nm are measured to be 4.29 and 3.03, respectively, and the group velocity dispersions of these two modes are ~3000 ps/nm/km and ~18000 ps/nm/km, respectively.

3.3. Loss measurement in waveguide circuits

Our point-to-point near-field OFDR can also measure losses of component waveguides in a complex circuit [Fig. 6(a)]. As discussed in Section 2.2, the information of the AFM tip position (L_1) and the ratio of the reflection and extinction components ($|E_r| = |E_{\mathrm{Sig1}}|/|E_{\mathrm{Sig2}}|$) can both be acquired from FT(η).

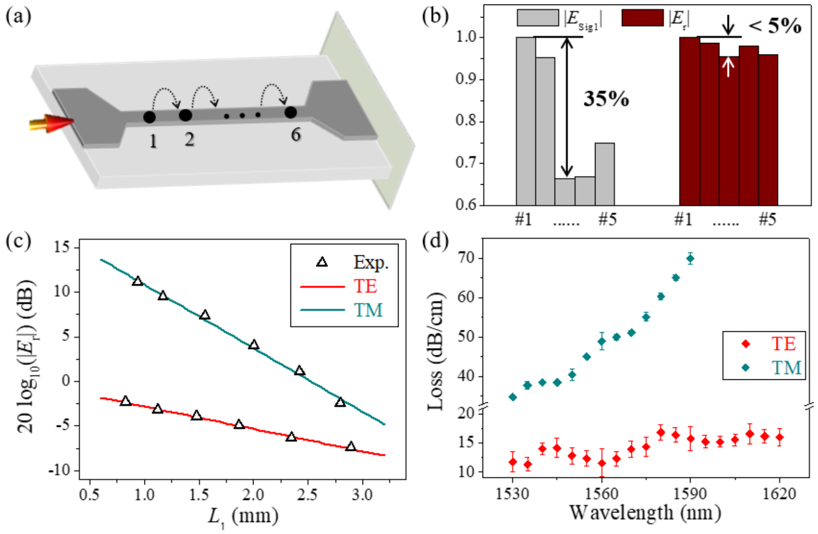

Fig. 6. (a) Sketch of point-to-point measurement of the propagation loss in a nano-waveguide. (b) Amplitudes of the light directly reflected by the tip ($|E_{\mathrm{Sig1}}|$) and the amplitude ratios of the reflection and the extinction lights ($|E_{\mathrm{r}}|$) at five trials. (c) Derivation of the propagation losses of the TE and TM modes at 1550 nm. The uncertainties of $|E_{\mathrm{r}}|$ at all the probe positions are smaller than the sizes of the dots. (d) Measured loss spectra of the TE and the TM modes. The error bars represent the standard deviations of the measured losses.

In experiment, the wavelength sweeping range of the laser is set to be 5 nm with the spacing to be 5 pm. Such a choice is a compromise considering both the wavelength dependence of the group index and loss of a nano-waveguide [35,36]. We also set the wavelength sweeping rate to be 0.5 nm/s, rendering each measurement to last for only ~10 s (thus the phase drift can be neglected). Because of avoiding raster scans of the AFM tip, our OFDR method shortens the measurement duration by one to two orders of magnitude than NSOM imaging method [3]. It is also noted that if a more accurate L_1 information is needed, an OFDR measurement across a wider wavelength range (e.g., 50 nm) can be taken.

3.3.1. Propagation losses of different segments of nano-waveguides

In order to check the repeatability, we carry out measurements for the TE and TM modes in the same nano-waveguide. With the variation of α_0 in Eq. (1) (mainly due to the change of the fiber-to-waveguide coupling), multiple measurements at a single site yield different $|E_{\mathrm{Sig1}}|$, whose variation is around 7 times greater than that of $|E_{\mathrm{r}}|$, as shown in Fig. 6(b). This experiment clearly validates that $|E_{\mathrm{r}}|$ as a measurand has superior resistance to the misalignment issue in a practical setup.

Placing the AFM tip at six different sites along one nano-waveguide, Fig. 6(c) shows the measured L_1 and $|E_{\mathrm{r}}|$. With linear fit, the propagation losses of the TE and TM modes at 1550 nm are derived to be 12.5 ± 0.8 dB/cm and 35.6 ± 2.1 dB/cm, respectively. Furthermore, Fig. 6(d) shows the measured loss spectra from 1530 to 1620 nm. In comparison with the almost flat loss spectrum in the TE polarization, the loss of the TM mode rises quickly toward 1600 nm, coinciding well with the cutoff wavelength estimation according to FEM simulation.

To analyze the loss measurement errors in Fig. 6(c), we classify them to four origins: 1) the variation of the quantity $|E_{\mathrm{r}}|$ in different measurements (< 0.2 dB), which is of course much smaller than that of $|E_{\mathrm{Sig1}}|$. Nevertheless, our FDTD simulation still implies that if the AFM tip deviates from the midpoint of the nano-waveguide by 20 nm (i.e., the resolution of a *s*-NSOM probe), the variation of $|E_\mathrm{r}|$ will reach the level of 1%; 2) the error of the measured time delay after FT (< 0.5%); 3) the error of the measured group indices (∼ 2%); 4) the variation of the factor $\alpha_\mathrm{refl}/\alpha_\mathrm{ext}$ caused by a 20 nm width variation of a nano-waveguide (∼ 0.5% according to FDTD simulation, Appendix A), which is inevitable during fabrication.

If a complex circuit is composed by several waveguides, our method can also measure the loss of each component waveguide. We first investigate a structure consisting of two nano-waveguides and a series of etched holes in between [Fig. 7(a)]. Near-field OFDR measurements are conducted at 4 sites. From the FT curves measured at sites 1# and 2#, the reflections from those etched holes and the rear facet are clearly visible [Fig. 7(b)]. In the TE polarization, the overall loss of the circuit can be divided into the losses of the two nano-waveguides (15.1 ± 1.1 dB/cm and 11.4 ± 0.8 dB/cm, respectively) and the insertion loss of the etched holes (4.2 ± 0.1 dB), as shown in Fig. 7(c) [37].

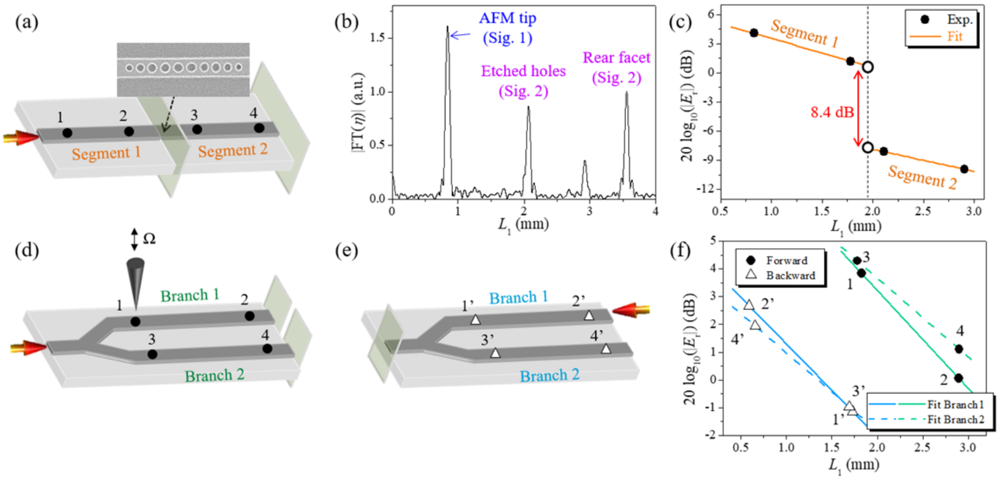

Fig. 7. (a,d,e) Schematic of loss measurements of two SOI nano-waveguides connected in series or in parallel. Inset in (a): SEM image of the etched holes in between. (b) FT of the spectrum of the demodulated signal η for the structure of (a) when the AFM tip is placed at site 1# and the launch light (at 1550 nm) is in the TE polarization. (c,f) Derivation of the component losses of different nano-waveguide segments in the series or the parallel configurations.

The second circuit to investigate is composed of two nominally identical nano-waveguides connected with a Y-junction. The AFM tip is also placed at four sites to measure the losses of different waveguide branches. As sketched in Fig. 7(d), any reflected light from the other branch waveguide can be eliminated out of the demodulation signal η (at the frequency of Ω). In the TE polarization, the measured losses of the two branch waveguides are 17.7 ± 0.8 dB/cm and 14.2 ± 0.8 dB/cm, respectively [the green solid and dashed curves in Fig. 7(f)]. When the measurement is conducted in the reverse direction [Fig. 7(e)], the losses of Branches 1 and 2 become 16.7 ± 1.3 dB/cm and 14.0 ± 1.1 dB/cm [the blue solid and dashed curves in Fig. 7(f)], respectively. The measurements in both directions agree well with each other. The differences of the losses of the two nano-waveguide branches (i.e., 3.5 dB/cm or 2.7 dB/cm, which is beyond our measurement precision) seem from their different qualities after long use. Further, our measurement will not be influenced by the qualities of the Y-junction and the tapered transitions, which is lacked in other loss measuring methods [12,13].

3.3.2. Silver nanowire as a deployable reflection plane

Owing to the adoption of $|E_{\mathrm{r}}|$, our loss measurements are premised on the reflection at the rear facet of the waveguide. To lift this restriction and extend this method to more complex circuits, a deployable and erasable nano-reflector is demanded. We use chemically synthesized silver nanowires (Ag NWs) [43] with the nominal diameter and length of ~300 nm and >10 µm, respectively. FDTD simulation shows that such an Ag NW on the top of a 500 nm × 220 nm SOI waveguide can give rise to light reflection on the order of 0.001 for both TE and TM modes at 1550 nm (Appendix B).

In experiment, we find a waveguide with a damaged rear facet [Fig. 8(a)], and all the other parameters of this waveguide are the same as in Fig. 3(a). After laying an Ag NW upon this nano-waveguide, the intersection angle is measured to be ~96°. Figure 8(b) shows the FT of the spectrum of η. The peaks arising from the reflection of the AFM tip and the Ag NW are clearly seen, while the reflection from the rear facet of the waveguide is invisible. With the aid of the light reflection by this Ag NW, our measurements yield the propagation losses of the TE and TM modes of 41.0 ± 2.4 dB/cm and 77.4 ± 5.5 dB/cm, respectively, at 1550 nm [Fig. 8(c)]. The high attenuation of this waveguide sample may be due to severe contamination and damage.

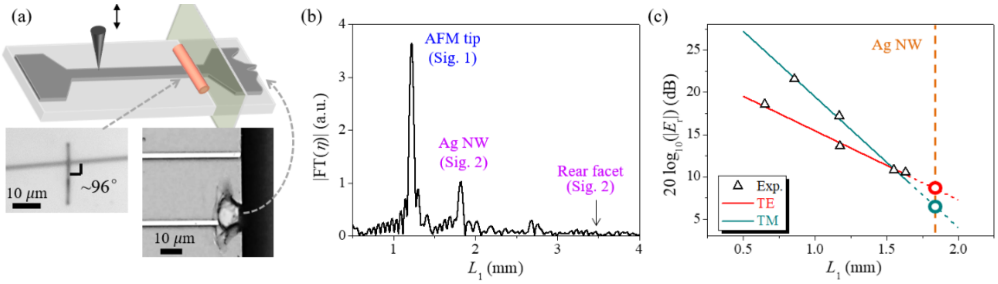

Fig. 8. (a) Schematic of laying an Ag NW atop a SOI nano-waveguide with a broken rear facet. Inset: Optical microscope images of the Ag NW and the rear facet. (b) FT of the spectrum of the demodulated signal η for the TE mode at ∼1550 nm. (c) Derivation of the losses of the TE and TM modes at 1550 nm. At the two hollow circles, $|E_{\mathrm{r}}|$ reads 2.7 and 2.2 for the TE and TM modes, respectively.

Since our Ag NW's are directly placed upon the nano-waveguide, the light reflection at that site can avoid the complexities arising from the light transmission through a linear taper and the intermodal interference in a multi-mode waveguide. The reflectivity (i.e., the return loss) of a perpendicularly-placed Ag NW can then be directly inferred. We linearly extend the curve of $20\times\log_{10}(|E_{\mathrm{r}}|)$ in Fig. 8(c) to the position of the Ag NW (i.e., $L_1 = L_2$). According to Eq. (2), the value $|E_{\mathrm{r}}|$ at that place should be equal to $\alpha_{\mathrm{refl}}/(2r\dot{c}\alpha_{\mathrm{ext}})$. Utilizing the FDTD simulated values of $\alpha_{\mathrm{refl}}/\alpha_{\mathrm{ext}} \approx 0.15$ (0.148) for the TE (TM) mode at 1550 nm (see Appendix A), we deduce the reflectivity (r^2) of the Ag NW to be 0.0008 (0.0011) for two polarizations. These experimentally derived results agree well with the FDTD simulation of a 300 nm-diameter Ag NW atop a 500 nm × 220 nm SOI nano-waveguide (Appendix B).

3.3.3. Propagation losses in multi-mode waveguides

The unique mode-resolving capability of our method can also be embodied in loss measurement. As depicted in Fig. 9(a), in a sample composed of a 2.15 mm multi-mode waveguide (2 µm × 220 nm) and a 1.85 mm single-mode waveguide (500 nm × 220 nm), we precisely lay the AFM tip on the midpoint along the waveguide. In order to distinguish different modes within a short distance, a wavelength sweeping range of 30 nm is adopted. As shown in Fig. 9(b), when the light is launched from the multi-mode waveguide side, six peaks corresponding to Signals

1 and 2 of $TM_{00}/TM_{01}/TM_{02}$ modes (with different group indices) are clearly visible in the FT curve of the η spectrum. The coexistence of these three TM modes can also be validated by our near-field imaging (see Fig. 4). From the Signal 2 peaks in Fig. 9(b) and the length of the multi-mode waveguide (2.15 mm), the group indices of TM_{00}, TM_{01}, and TM_{02} modes are estimated to be 3.6, 3.8, and 4.0, respectively.

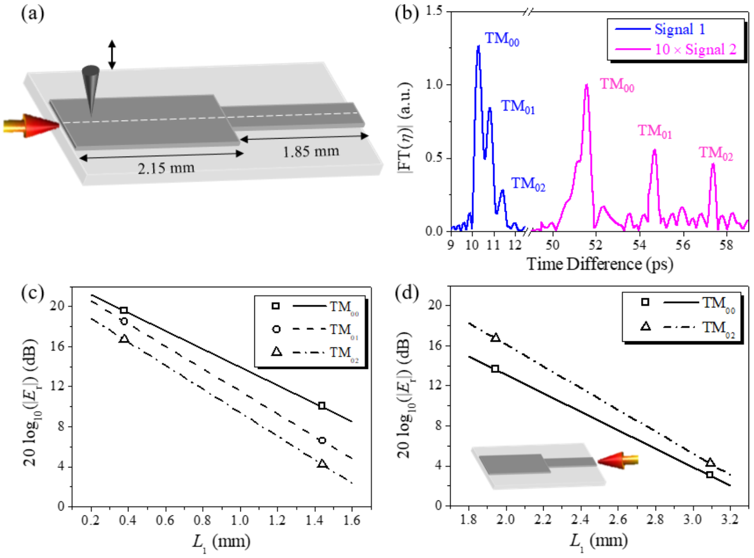

Fig. 9. (a) Schematic of measurement along a multi-mode waveguide. (b) FT of the spectrum of the demodulated signal η. (c,d) Derivation of the propagation losses of the three TM modes at 1550 nm when light is launched from the two sides, respectively. The symbols are the measured results, and the lines are linear fits.

Using the method of measuring $|E_r|$ at different probe sites and assuming that the intermodal coupling during propagation can be neglected, the measured losses of TM_{00}, TM_{01}, and TM_{02} modes are 38.4 ± 1 dB/cm, 42.3 ± 2.1 dB/cm, and 54.5 ± 3 dB/cm, respectively [Fig. 9(c)]. The measurement accuracy is restricted by the short waveguide length. If the light is launched from the single-mode waveguide side, only the TM_{00} and TM_{02} modes can be excited because of the mode symmetry. Figure 9(d) shows the loss measurement of these two modes, and the results of 38.1 ± 1 dB/cm and 52.4 ± 3 dB/cm coincide well with the results of Fig. 9(c).

4. Discussion and conclusion

In this work, we study in detail an all-fiber reflection-based s-NSOM for a wide range of on-chip characterization applications. Thanks to the sharp tip and the piezoelectric position control of a s-NSOM, the resolving power in topographic and optical imaging can be utilized to provide comprehensive information of a nano-photonic circuit. The all-fiber and single fiber-to-chip coupling configuration of our setup brings about a convenience and good tolerance for optical alignment. Our waveguide-based light collection strategy assures an efficient near-field signal acquisition and a low background noise.

In the heterodyne detection scheme, the issues restricting accurate phase measurements, e.g., the temperature and stress induced random drifts in a fiber interferometer, have been overcome by phase compensation in a CPI design. The excellently low phase noise is the guarantee for stable phase imaging within a typical raster-scanning duration of 10 minutes.

Further, frequency sweeping opens another dimension rather than lateral raster-scanning for optical characterizations. In many circumstances, frequency sweeping is more stable and faster than mechanical movement. More importantly, the employment of the OFDR technique can extend the near-field characterization capability out of a single raster-scanning frame. In this manner, a point-to-point reflectometric measuring scheme successfully combines the flexibility of probe positioning, the amplitude and phase characteristics of reflection signal, and orders of magnitude shorter measurement duration [15,37]. Besides, the analysis and utilization of the two different reflection components help to dramatically reduce the measurement errors caused by environmental fluctuations and fabrication imperfections.

In summary, we propose and experimentally validate a convenient and high-stability phase, group index, group velocity dispersion, and loss measuring technique for on-chip circuits. Using an all-fiber reflection-based *s*-NSOM, the heterodyne phase detection has demonstrated an ultralow drift rate of ~ 0.013°/s. Flexible characterizations of group index, group velocity dispersion, and loss (return loss) can be applied to each nano-waveguide segment of a circuit with a typical uncertainty of propagation loss of ~1 dB/cm for a 0.2 cm long waveguide. Our near-field point-to-point frequency-domain reflectometric method assisted by a deployable Ag NW provides a characterization solution for more complex photonic circuits.

APPENDIX A: FDTD simulations of light interactions with AFM tip (α_{refl} & α_{ext})

If an AFM tip (made of silicon and with the tip radius of 10 nm and the full cone angle of 30°) lies vertically upon the midpoint of a 500 nm × 220 nm waveguide, the induced light reflection and extinction can be simulated by FDTD method. Figure 10(a) shows the spectra of the amplitude coefficients α_{refl} and α_{ext}, manifesting two wavelength-insensitive $\alpha_{\text{refl}}/\alpha_{\text{ext}}$ of ~0.15 and ~0.148 for the TE and TM modes within the wavelength range of interest, respectively.

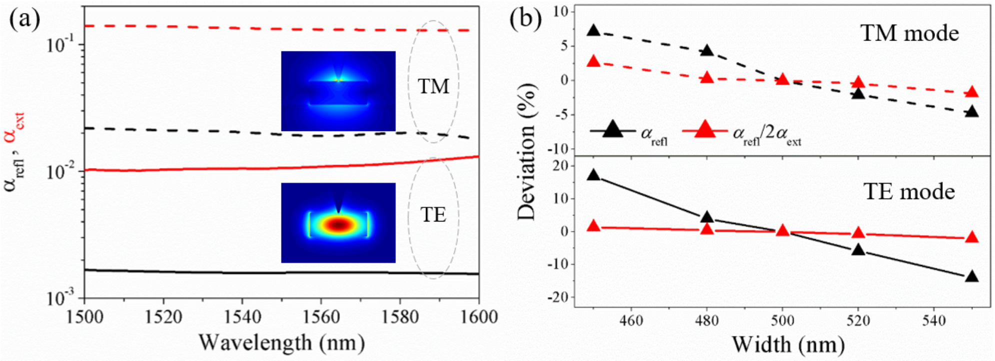

Fig. 10. (a) FDTD simulated α_{refl} (black curves) and α_{ext} (red curves) for the TE and TM modes, respectively, when an AFM tip is placed on the midpoint. (b) FDTD simulated deviations of α_{refl} and $\alpha_{\text{refl}}/2\alpha_{\text{ext}}$ with the width of the nano-waveguide for the TE and TM modes. Inset in (a): $|E|^2$ distributions at 1550 nm monitored in the cross-sectional planes containing the AFM tip.

Additionally, Fig. 10(b) shows the simulated variations of α_{refl} and α_{ext} with the width of the nano-waveguide. Hypothesizing that the precision of nano-fabrication is limited on the level of ±20 nm, the resultant deviation of $\alpha_{\text{refl}}/(2\alpha_{\text{ext}})$ is estimated to be around ±0.5% for both TE and TM modes, better than the deviation of α_{refl}. It is because the influences of the waveguide width to α_{refl} and α_{ext} have the same trend, thus partly canceling out with each other. According to Eqs. (1) and (2), this attribute is in favor of the adoption of the measurand $|E_{\text{r}}|$.

APPENDIX B: Precisely laying an Ag NW atop a SOI nano-waveguide

Figure 11(a) shows how to use a tapered glass tube connected with a μ-manipulator (Narishige, MMO-202ND) to pick up an Ag NW, and then to place it on the top of a SOI waveguide with an accurate intersection angle. The chemically synthesized Ag NWs have a nominal diameter of 300 nm and length of >10 μm [43]. After loss measurements, these Ag NW's can be removed.

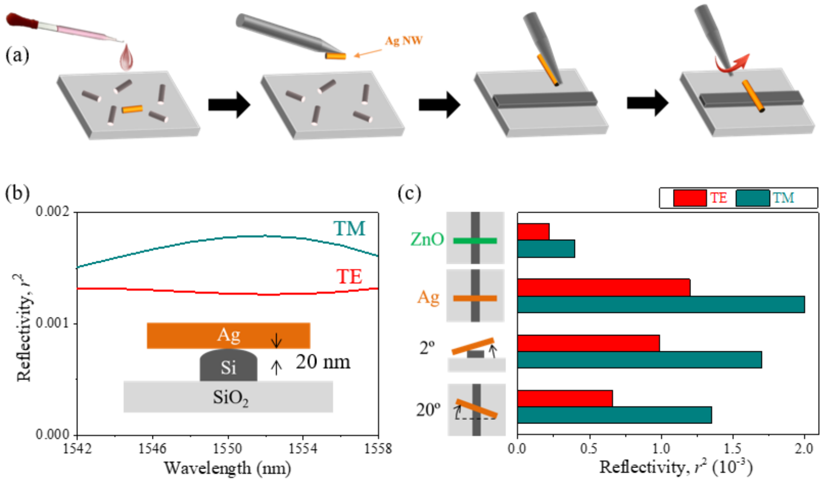

Fig. 11. (a) Flow chart of placing an Ag NW atop a nano-waveguide. (b) Simulated reflectivity (r^2) by a 300 nm diameter Ag NW atop a 500 nm × 220 nm SOI waveguide. (c) Simulated reflectivity by a ZnO NW ($d = 300$ nm) and an Ag NW ($d = 300$ nm) at 1550 nm.

Figure 11(b) shows the FDTD simulated reflectivity's of a 500 nm × 220 nm SOI waveguide by a perpendicularly-aligned Ag NW for the TE and TM modes. In the simulation, a slightly curved top surface (with the bulge of 20 nm) is considered to embody the real structure. It is seen that r^2 is in the 0.001 level for both two polarizations. Once the material of the NW changes to a dielectric (e.g., ZnO with the refractive index of 2.45), the reflectivity drops to less than 0.0005 [Fig. 11(c)]. Figure 11(c) also calculates the influences of different intersection angles between Ag NW and nano-waveguide.

Funding. National Natural Science Foundation of China (62075083, 12074421, 11774413); Fundamental Research Funds for the Central Universities (21620316); Guangzhou Science and Technology Program (202201010460); National Key Research and Development Program of China (2017YFA0303800); Strategic Priority Research Program of Chinese Academy of Sciences (XDB33000000).

Acknowledgments. The authors would like to thank Dr. Lin Ge for the help in the AFM operation.

Disclosures. The authors declare no conflicts of interest.

Data availability. Data underlying the results presented in this paper are not publicly available at this time but may be obtained from the authors upon reasonable request.

References

1. D. W. Pohl, W. Denk, and M. Lanz, "Optical stethoscopy: Image recording with resolution λ/20," Appl. Phys. Lett. **44**(7), 651–653 (1984).
2. Y. Inouye and S. Kawata, "Near-field scanning optical microscope with a metallic probe tip," Opt. Lett. **19**(3), 159–161 (1994).
3. N. Rotenberg and L. Kuipers, "Mapping nanoscale light fields," Nat. Photonics **8**(12), 919–926 (2014).
4. B. J. Shastri, A. N. Tait, T. Ferreira de Lima, W. H. Pernice, H. Bhaskaran, C. D. Wright, and P. R. Prucnal, "Photonics for artificial intelligence and neuromorphic computing," Nat. Photonics **15**(2), 102–114 (2021).
5. E. Pelucchi, G. Fagas, I. Aharonovich, D. Englund, E. Figueroa, Q. Gong, H. Hannes, J. Liu, C. Lu, N. Matsuda, J. Pan, F. Schreck, F. Sciarrino, C. Silberhorn, J. Wang, and K. D. Jöns, "The potential and global outlook of integrated photonics for quantum technologies," Nat. Rev. Phys. **4**(3), 194–208 (2022).

6. S. Arora, T. Bauer, R. Barczyk, E. Verhagen, and L. Kuipers, “Direct quantification of topological protection in symmetry-protected photonic edge states at telecom wavelengths,” Light: Sci. Appl. **10**(1), 9 (2021).
7. C. Lu, Y. Sun, C. Wang, H. Zhang, W. Zhao, X. Hu, M. Xiao, W. Ding, Y. Liu, and C. T. Chan, “On-chip nanophotonic topological rainbow,” Nat. Commun. **13**(1), 2586 (2022).
8. Z. Liu, X. Liu, Z. Xiao, C. Lu, H. Wang, Y. Wu, X. Hu, Y. Liu, H. Zhang, and X. Zhang, “Integrated nanophotonic wavelength router based on an intelligent algorithm,” Optica **6**(10), 1367–1373 (2019).
9. X.-T. He, E.-T. Liang, J.-J. Yuan, H.-Y. Qiu, X.-D. Chen, F.-L. Zhao, and J.-W. Dong, “A silicon-on-insulator slab for topological valley transport,” Nat. Commun. **10**(1), 1–9 (2019).
10. K. Li, X. Cao, Y. Wan, G. Wu, and J. Wang, “Fundamental analyses of fabrication-tolerant high-performance silicon mode (de)multiplexer,” Opt. Express **30**(13), 22649–22660 (2022).
11. K. Gallacher, R. W. Millar, D. J. Paul, J. Frigerio, A. Ballabio, G. Isella, F. Rusconi, P. Biagioni, V. Giliberti, A. Sorgi, L. Baldassarre, and M. Ortolani, “Characterization of integrated waveguides by atomic-force-microscopy-assisted mid-infrared imaging and spectroscopy,” Opt. Express **28**(15), 22186–22199 (2020).
12. Y. A. Vlasov and S. J. McNab, “Losses in single-mode silicon-on-insulator strip waveguides and bends,” Opt. Express **12**(8), 1622–1631 (2004).
13. R. Regener and W. Sohler, “Loss in low-finesse Ti:LiNbO$_3$ optical waveguide resonators,” Appl. Phys. B **36**(3), 143–147 (1985).
14. B. J. Soller, D. K. Gifford, M. S. Wolfe, and M. E. Froggatt, “High resolution optical frequency domain reflectometry for characterization of components and assemblies,” Opt. Express **13**(2), 666–674 (2005).
15. A. Bruyant, G. Lerondel, S. Blaize, I. Stefanon, S. Aubert, R. Bachelot, and P. Royer, “Local complex reflectivity in optical waveguides,” Phys. Rev. B **74**(7), 075414 (2006).
16. L. Novotny and B. Hecht, *Principles of Nano-Optics* (Cambridge University, 2006).
17. Y. Sonnefraud, N. Chevalier, J.-F. Motte, S. Huant, P. Reiss, J. Bleuse, F. Chandezon, M. T. Burnett, W. Ding, and S. A. Maier, “Near-field optical imaging with a CdSe single nanocrystal-based active tip,” Opt. Express **14**(22), 10596–10602 (2006).
18. S. Kim, N. Yu, X. Ma, Y. Zhu, Q. Liu, M. Liu, and R. Yan, “High external-efficiency nanofocusing for lens-free near-field optical nanoscopy,” Nat. Photonics **13**(9), 636–643 (2019).
19. M. Burresi, D. van Oosten, T. Kampfrath, H. Schoenmaker, R. Heideman, A. Leinse, and L. Kuipers, “Probing the magnetic field of light at optical frequencies,” Science **326**(5952), 550–553 (2009).
20. F. Huth, A. Chuvilin, M. Schnell, I. Amenabar, R. Krutokhvostov, S. Lopatin, and R. Hillenbrand, “Resonant antenna probes for tip-enhanced infrared near-field microscopy,” Nano Lett. **13**(3), 1065–1072 (2013).
21. W. Bao, M. Melli, N. Caselli, F. Riboli, D. S. Wiersma, M. Staffaroni, H. Choo, D. F. Ogletree, S. Aloni, J. Bokor, S. Cabrini, F. Intonti, M. B. Salmeron, E. Yablonovitch, P. J. Schuck, and A. Weber-Bargioni, “Mapping local charge recombination heterogeneity by multidimensional nanospectroscopic imaging,” Science **338**(6112), 1317–1321 (2012).
22. L. Sun, B. Bai, X. Meng, T. Cui, G. Shang, and J. Wang, “Near-field probing the magnetic field vector of visible light with a silicon nanoparticle probe and nanopolarimetry,” Opt. Express **26**(19), 24637–24652 (2018).
23. H. G. Frey, F. Keilmann, A. Kriele, and R. Guckenberger, “Enhancing the resolution of scanning near-field optical microscopy by a metal tip grown on an aperture probe,” Appl. Phys. Lett. **81**(26), 5030–5032 (2002).
24. J. Li, J. Mu, B. Wang, W. Ding, J. Liu, H. Guo, W. Li, C. Gu, and Z. Li, “Direct laser writing of symmetry-broken spiral tapers for polarization-insensitive three-dimensional plasmonic focusing,” Laser Photonics Rev. **8**(4), 602–609 (2014).
25. F. B. Arango, F. Alpeggiani, D. Conteduca, A. Opheij, A. Chen, M. I. Abdelrahman, T. F. Krauss, A. Alù, F. Monticone, and L. Kuipers, “Cloaked near-field probe for non-invasive near-field optical microscopy,” Optica **9**(7), 684–691 (2022).
26. W. C. L. Hopman, A. J. F. Hollink, R. M. de Ridder, K. O. van der Werf, V. Subramaniam, and W. Bogaerts, “Nano-mechanical tuning and imaging of a photonic crystal micro-cavity resonance,” Opt. Express **14**(19), 8745–8752 (2006).
27. J. T. Robinson, S. F. Preble, and M. Lipson, “Imaging highly confined modes in sub-micron scale silicon waveguides using transmission-based near-field scanning optical microscopy,” Opt. Express **14**(22), 10588–10595 (2006).
28. Y. Sun, B. Wang, R. Salas-Montiel, S. Blaize, R. Bachelot, L. Feng, and W. Ding, “Imaging of guided waves using an all-fiber reflection-based NSOM with self-compensation of a phase drift,” Opt. Lett. **43**(20), 4863–4866 (2018).
29. I. Stefanon, S. Blaize, A. Bruyant, S. Aubert, G. Lerondel, R. Bachelot, and P. Royer, “Heterodyne detection of guided waves using a scattering-type scanning near-field optical microscope,” Opt. Express **13**(14), 5553–5564 (2005).
30. N. Ocelic, A. Huber, and R. Hillenbrand, “Pseudoheterodyne detection for background-free near-field spectroscopy,” Appl. Phys. Lett. **89**(10), 101124 (2006).
31. M. L. M. Balistreri, J. P. Korterik, L. Kuipers, and N. F. van Hulst, “Local observations of phase singularities in optical fields in waveguide structures,” Phys. Rev. Lett. **85**(2), 294–297 (2000).
32. A. H. Hartog, A. J. Conduit, and D. N. Payne, “Variation of pulse delay with stress and temperature in jacketed and unjacketed optical fibres,” Opt. Quantum Electron. **11**(3), 265–273 (1979).
33. M. Wulf, D. M. Beggs, N. Rotenberg, and L. Kuipers, “Unravelling nonlinear spectral evolution using nanoscale photonic near-field point-to-point measurements,” Nano Lett. **13**(12), 5858–5865 (2013).

34. J. M. Stiegler, A. J. Huber, S. L. Diedenhofen, J. Gomez Rivas, R. E. Algra, E. Bakkers, and R. Hillenbrand, “Nanoscale free-carrier profiling of individual semiconductor nanowires by infrared near-field nanoscopy,” Nano Lett. **10**(4), 1387–1392 (2010).
35. D. Zhao, D. Pustakhod, K. Williams, and X. Leijtens, “High resolution optical frequency domain reflectometry for analyzing intra-chip reflections,” IEEE Photonics Technol. Lett. **29**(16), 1379–1382 (2017).
36. L. A. Bru, D. Pastor, and P. Muñoz, “Integrated optical frequency domain reflectometry device for characterization of complex integrated devices,” Opt. Express **26**(23), 30000–30008 (2018).
37. Y. Sun, W. Ding, B. Wang, R. Salas-Montiel, S. Blaize, R. Bachelot, Z. Fan, and L. Feng, “Standing-wave spectrometry in silicon nano-waveguides using reflection-based near-field scanning optical microscopy,” Chin. Phys. B **28**(1), 010702 (2019).
38. L. Stern, B. Desiatov, I. Goykhman, G. M. Lerman, and U. Levy, “Near field phase mapping exploiting intrinsic oscillations of aperture NSOM probe,” Opt. Express **19**(13), 12014–12020 (2011).
39. M. L. M. Balistreri, J. P. Korterik, L. Kuipers, and N. F. van Hulst, “Phase mapping of optical fields in integrated optical waveguide structures,” J. Lightwave Technol. **19**(8), 1169–1176 (2001).
40. X. Wu, L. Sun, J. Wang, and Q. Tan, “Real-time phase error compensation in phase sensitive scanning near-field optical microscopy,” Appl. Opt. **54**(19), 6128–6133 (2015).
41. G. M. Ponzo, M. N. Petrovich, X. Feng, P. Horak, F. Poletti, P. Petropoulos, and D. J. Richardson, “Fast and Broadband fiber dispersion measurements with dense wavelength sampling,” Opt. Express **22**(1), 943–953 (2014).
42. J. Komma, C. Schwarz, G. Hofmann, D. Heinert, and R. Nawrodt, “Thermo-optic coefficient of silicon at 1550 nm and cryogenic temperatures,” Appl. Phys. Lett. **101**(4), 041905 (2012).
43. Y. Sun and Y. Xia, “Large-scale synthesis of uniform silver nanowires through a soft, self-seeding, polyol process,” Adv. Mater. **14**(11), 833–837 (2002).

159.226.36.252 {ts '2022-10-25 23:24:27'}